Designing Multi-DoF Epidermal Bend Sensors Using Flexible Resistive Traces

Jiakun Yu, Hasindu Kariyawasam, *Graduate Student Member, IEEE*, Shuying Wu, Sriram Subramanian, and Anusha Withana, *Associate Member, IEEE*

***Abstract*—We present a single-layer resistive epidermal bend sensor that senses four degrees of freedom (DoFs) via combinatorial port connections within a unified pattern, avoiding multisensor arrays. We instantiate and compare four patterns (square-like, tree-like, arc-like, and honeycomb-like) under a common single-layer measurement strategy; we present modeling for the straight layout and empirical analyses for the others. With a 15:100 carbon-to-gel composite and a 0.3-mm conductive layer after 20% prestrain, the material exhibits hysteresis of 0.6% and an average gauge factor (GF) magnitude of 0.6. The proposed design is thin, flexible, and conforms comfortably to the skin. Across test sets, 95.4% of angle estimates fall within ±2.798° of ground truth. Our approach utilizes cost-effective materials and accessible fabrication techniques. This article demonstrates the potential of our method for various applications in epidermal sensing. We envision that the proposed resistive patterns will help designers to create accurate, conformal, and multi-DoF sensors.**

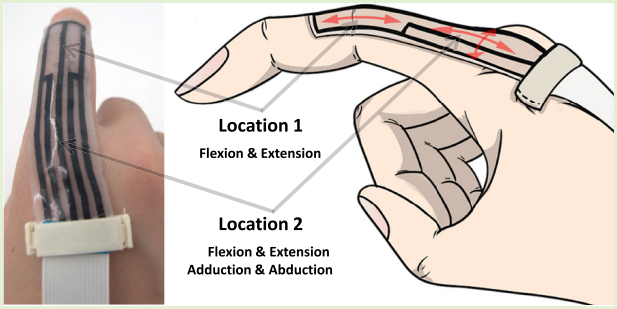

***Index Terms*— Epidermal sensor, fabrication, multi-degree of freedom (multi-DoF), pattern designs, soft sensors.**

Received 23 September 2025; accepted 14 October 2025. Date of publication 23 October 2025; date of current version 1 December 2025. This work was supported in part by Australian Research Council Discovery Early Career Award (DECRA) under Grant DE200100479; in part by the University of Sydney's Digital Sciences Initiative through the Digital Sciences Initiative (DSI) Research Pilot Project Grant Scheme; and in part by the Neurodisability Assist Trust and Cerebral Palsy Alliance, Australia, under Grant PRG04219. The work of Anusha Withana was supported by DECRA funded by Australian Government. The associate editor coordinating the review of this article and approving it for publication was Prof. Wei-Chen Huang. *(Corresponding author: Jiakun Yu.)*

This work involved human subjects or animals in its research. Approval of all ethical and experimental procedures and protocols was granted by the Human Research Ethics Committee of the University of Sydney under Approval No. 2019/553.

Jiakun Yu is with the School of Computer Science, The University of Sydney, Sydney, NSW 2006, Australia, and also with the Department of Computer Science, Purdue University, West Lafayette, IN 47906 USA (e-mail: jiakun.yu@sydney.edu.au).

Hasindu Kariyawasam is with the School of Computer Science, The University of Sydney, Sydney, NSW 2006, Australia, and also with the Department of Electronics and Telecommunication Engineering, University of Moratuwa, Moratuwa 10400, Sri Lanka (e-mail: khpiyumantha@gmail.com).

Shuying Wu is with the School of Aerospace, Mechanical and Mechatronic Engineering, The University of Sydney, Sydney, NSW 2006, Australia (e-mail: shuying.wu@sydney.edu.au).

Sriram Subramanian is with the Department of Computer Science, University College London, WC1E 6BT London, U.K. (e-mail: s.subramanian@ucl.ac.uk).

Anusha Withana is with the School of Computer Science and Sydney Nano Institute (Sydney Nano), The University of Sydney, Sydney, NSW 2006, Australia (e-mail: anusha.withana@sydney.edu.au).

Digital Object Identifier 10.1109/JSEN.2025.3623068

I. Introduction

ADVANCEMENTS in bodily deformation sensing have facilitated novel applications in health [1], [2], [3], accessibility [4], [5], sports [6], [7], and virtual reality [8], [9], [10]. For example, joint moment sensing in robot-assisted fingers aids in the training of chronic stroke survivors [11]. Muscle deformations are increasingly involved in metaverse somatosensory interactions [12]. Sign language recognition systems use finger movement sensing to assist individuals who are deaf and hard-of-hearing [4]. These on-body movements, especially subtle biomechanical deformations, are typically measured by wearable devices due to their high accuracy [13]. In addition, wearables are resilient to occlusion, making them suitable for monitoring movements even when visual tracking is compromised [14]. As wearable technology advances, there is a growing need among users for nonintrusive, soft, and skin-friendly wearables [15], [16], [17]. Epidermal devices are a typical example of such technology [18], [19]. The effectiveness of epidermal sensors largely depends on the substrate material. Their flexibility, stretchability, and biocompatibility are essential for conforming to the contours and movements of human skin [18], [20], facilitating natural accommodation to the skin's dynamic nature. This approach ensures both user comfort and effective sensor performance. Key inherently soft materials for epidermal sensors include hydrogels [20], polydimethylsiloxane (PDMS) [18], [21], and tattoo decal

paper [22], [23]. In our work, we opted for Platsil Gel-0030,[1] a two-part, platinum-catalyzed silicone, which was selected for its greater local availability, lower cure or demold time, and higher softness compared with Sylgard[2] 184, one of the widely used PDMS.

However, conventional soft strain gauges that can be placed on the body as epidermal sensors commonly focus on uniaxial sensing [24], [25], although body movements are inherently multi-degrees of freedom (multi-DoFs) due to complex motions of joints and the flexibility of the skin that allows stretching, bending, and deformations. Uniaxial sensors only capture stretching or compression in one direction, which limits their application in capturing natural, complex movements (e.g., hand or joint articulation). Motivated by this, we developed multi-DoF deformation sensors that enable a more accurate representation of these complex movements and deformations.

In addition, recent development of deformable sensors has seen a variety of pattern designs, each tailored to enhance the sensor performance. Resistive sensing has evolved from simple loops and linear strain patterns [26], [27] to 2-D geometries such as zigzag [28], [29], serpentine [30], [31], and space-filling/fractal curves [32]. These patterned traces create direction-dependent current paths and produce larger, direction-dependent ΔR while remaining thin and conformal, but most of them can only sense a single point. In parallel, direction-sensitive resistive materials generate distinct resistance changes for orthogonal bending [33], [34]. Although thin and sensitive, such film-based designs also typically operate at one location and may require special processing. In contrast, we use commodity resistive composites in a single layer, unified trace network and achieve multilocation sensing through combinatorial port connections. This preserves epidermal conformality, reduces wiring and calibration, and enables recovery of two in-plane bending axes at two spatial locations on the same sheet—without multilayer stacks or discrete sensor arrays. For example, capacitive stacks can also realize multi-DoF using dense, sparse, or misaligned electrodes [35], [36], [37], [38], but they generally require two conductive layers and thicker stacks.

Moreover, the sensors in our project are crafted using rapid, cost-effective fabrication methods and materials. There are various fabrication methods for epidermal sensors that have been previously developed, each tailored to the specific requirements of soft materials and intricate designs. In additive methods, recent human–computer interaction research has showcased screen printing for its precision and multifunctionality [39], [40], [41], inkjet printing for its ease of use and adaptability to conventional printers [42], [43], and direct on-skin printing for its ability to apply layers directly onto the skin [44], [45]. Subtractive techniques, such as laser cutting with CO_2 and UV lasers, offer precision in material shaping [46], [47], complemented by the simpler yet effective mechanical plotter cuts [48]. Mixed methods, combining elements of both additive and subtractive techniques, are exemplified by approaches that merge cutting and material transfer for the physical realization of digital designs [49], [50]. Our work utilizes a mixed-methods approach. Meanwhile, we streamline the fabrication process to enhance accessibility and efficiency. By leveraging standard fabrication tools like laser cutters, we achieved a thickness of 900 μm.

In general, our work introduces multi-DoF epidermal bend sensors via resistive sensing patterns. To best of the authors' knowledge, this is the first single-layer resistive multi-DoF epidermal bend sensing approach that achieves four DoF via combinatorial port connections within a unified pattern, avoiding complex multisensor arrays. Compared to prior approaches, the proposed designs provide three advantages: fewer conductive layers than capacitive sensing mechanisms [18], more DoFs than conventional strain gauges [30], and more deformation analysis through multi-data measurements rather than single-data measurements [51]. We propose four resistive pattern designs—square-like, tree-like, arc-like, and honeycomb—which enable multidirectional sensing at multiple locations. Each pattern has two sensing locations (top and bottom), and each location can sense two DoFs (x- and y-axes). Our sensor effectively demonstrated its capability to sense multi-DoF deformation across multiple sensing locations accurately. Specifically, we showcased a four-DoF sensor that achieves 95.4% accuracy with a tolerance of 2.798°. Moreover, we used the prestrained strategy to compensate for the nonmonotonic effect of the carbon-doped elastomer sensor. We also conducted finite element analysis and fatigue tests to assess measurement changes across various patterns. The results were verified using our test setup.

The main contributions of this article are as follows.

1) Developed unified resistive patterns that enable multi-DoF sensing in epidermal bend sensors, eliminating the need for multisensor arrays.
2) Introduced a cost-effective and easily replicable fabrication method for fast-prototyping epidermal sensors.
3) Provided comprehensive experimental validation and derived formulas for the proposed multi-DoF designs.

II. Theory of Operation

Our design draws inspiration from fractal geometric patterns observed in biological systems [52], [53], [54], which often exhibit self-similar characteristics. While such patterns have been studied in 3-D networks [55], [56], we adapt these concepts to create deterministic 2-D patterns for stretchable electronics. The resulting designs provide functional advantages through their hierarchical structure.

Fig. 1(e)–(h) shows our square pattern design, where smaller sections mirror the geometry of the whole structure. The design includes five connection ports and two distinct sensing locations, as shown in Fig. 1(f). This enables resistance measurements between each pair of ports, resulting in a total of ten measurements within a few microseconds. This rapid data acquisition allows for the detection of both lateral and vertical deformations in each sensing location by analyzing resistance variations and extracting relevant data

[1] www.barnes.com.au/product/platsil-gel-0030-prosthetic-grade-silicone/
[2] Registered trademark.

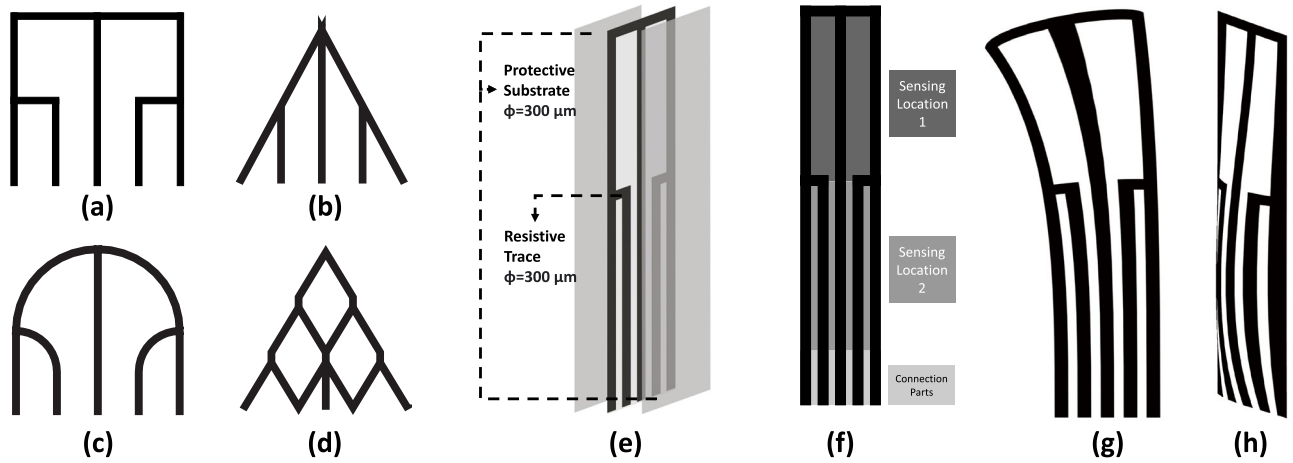

Fig. 1. (a)–(d) Four multi-DoF trace designs. (e) Overview of the sensor layers layout. (f) Detailed view of sensing locations and connection parts. (g) Lateral bending in sensing locations 1. (h) Vertical bending in sensing locations 2.

features. By integrating additional branch pairs and connection ports, we can scale our design to include more sensing locations, thereby enhancing the sensor's adaptability for complex deformation detection scenarios. We evaluated several pattern variations, including tree-like [see Fig. 1(b)], arc-like [see Fig. 1(c)], and honeycomb structures [see Fig. 1(d)] to determine the most effective configuration. Further details on the sensing mechanisms are discussed in Section IV.

III. Fabrication

This section outlines the development of our sensor, with a focus on the fabrication process and the selection of materials. In this sensor fabrication, two key types of materials are essential: substrate materials, which provide structural support and insulation, and conductive materials, which enable electrical resistance changes and signal transmission.

A. Substrate Materials

Substrate materials are critical in epidermal sensor design, offering insulation while maintaining flexibility and skin compatibility. They form the sensor's base, supporting conductive elements and ensuring safety and comfort when in contact with skin. We sought a substrate that balances these needs with ease of fabrication. PDMS, frequently used in soft electronics, initially seemed suitable but posed several challenges, including a complex mixing ratio, extended curing time, and limited availability [57]. To address these issues, we selected Platsil Gel-0030, a platinum-catalyzed silicone that cures to a milky white, Shore 0030 rubber. It offers a simpler 1:1 mixing ratio, a shorter 4-h curing time, and a skin-like hardness comparable to PDMS, while being more accessible from local suppliers, streamlining our laboratory fabrication process [58].

B. Conductive Mixtures

Conductive materials in the sensor transmit electrical signals, which are crucial for sensing capabilities. They must be effective conductors and also integrate seamlessly with the substrate. We used cost-effective acetylene carbon black powder (Alfa Aesar) as the conductive material, compared to alternatives like GaIn alloy and silver ink [18]. We prepared the conductive traces by first mixing the carbon powder with isopropyl alcohol and then combining it with Platsil at a 15:100 carbon/gel weight ratio. The alcohol reduces viscosity during mixing and evaporates during curing, preserving conductivity. We maintained a 0.3-mm layer thickness, with these parameters optimized and validated through testing (Section V-A). Fig. 2(b) illustrates the mixing process.

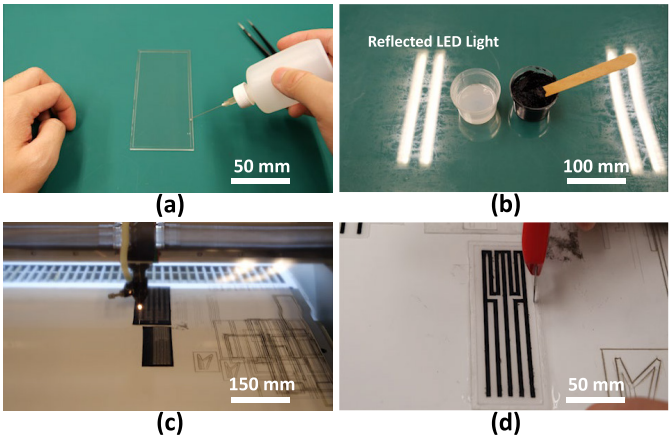

Fig. 2. (a) 300-μm acrylic sheet, laser cut into a frame, is glued onto a 2000-μm acrylic base to create the molding frame. (b) Preparation of the Platsil mixture (left) for combination with the carbon-isopropyl alcohol mixture (right). (c) Laser cutting of the cured conductive substrates to form conductive traces. (d) Final sensors were sealed with nonconductive Platsil mixtures on both sides, followed by demolding.

C. Procedure

Our fabrication process, inspired by Weigel et al. [18], Glauser et al. [36], and Tavakoli et al. [59], has been refined for standard laboratory resources and requirements, ensuring practicality in different fabrication needs.

We prepared two acrylic sheets: a thicker 2000-μm sheet for the mold base and a thinner 300-μm sheet for layer thickness

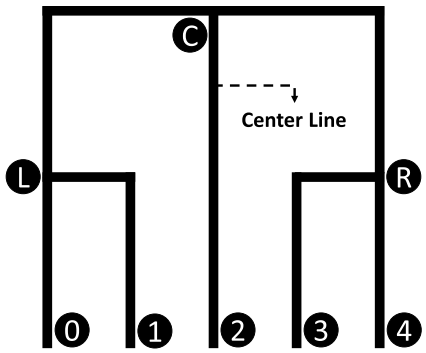

Fig. 3. Multi-DoF design schematic. Labels 0–4: connection points; L, C, and R: left, center, and right junctions, respectively.

control. After laser cutting the thinner sheet, it was used as a frame and glued onto the base using acrylic glue[3] as shown in Fig. 2(a). The carbon-doped Platsil mixture was poured into this mold, leveled with a rigid acrylic piece, and left to cure, forming a conductive substrate. This substrate was then cut using a laser cutter (LOTUS Blu60), which was set to a speed of 55 mm/s and a power of 12 W, as depicted in Fig. 2(c). The conductive traces were cleaned with isopropyl alcohol.

The sensor's three-layer structure was completed by pouring nonconductive Platsil around the conductive traces. The protective layers were cast using a metal plate base and acrylic sheet frames, with the conductive trace placed between them. As shown in Fig. 2(d), each layer was cured separately to ensure a smooth finish.

This fabrication process effectively addresses the challenges of creating flexible, skin-friendly, and electrically insulated sensors, suitable for a variety of applications.

IV. Understanding Multi-DoF Resistive Traces

We observed that resistance does not proportionally correlate with elongation in Section V-A, which could be the changes in area and resistivity during stretching. Before digging into the more complex multi-DoF design, we employed a square design as a prototype for analysis. We calculated the relationship between percentage elongation ($\Delta\ell/\ell$) and resistance changes between any two connection points. These elongation data serve as features for predicting 2-D deformation in each sensing location.

As depicted in Fig. 3, the square multi-DoF sensor design comprises five connection points (labeled 0–4), enabling resistance measurements between each pair of points. This setup yields ten distinct resistance measurements: R_{01}, R_{02}, R_{03}, R_{04}, R_{12}, R_{13}, R_{14}, R_{23}, R_{24}, and R_{34}, where R_{xy} represents the resistance measured between two points x and y. The conductive traces on both sides of the center line are segmented into three subsegments. These traces are denoted as $LC + C2 \rightarrow L2$, $L1$, and $L0$ with their resistances R_{L2}, R_{L1}, and R_{L0} and $RC + C2 \rightarrow R2$, $R3$, and $R4$ with their resistances R_{R2}, R_{R3}, and R_{R4} in Fig. 3. These subsegments can simplify data models and help designers and users understand the concept of multi-DoF sensing. We noticed that these subsegments and overall resistance measurements from the contact points have the relationships described as follows:

$$R_{L2} = \frac{1}{2}(R_{02} + R_{12} - R_{01}) \qquad R_{R2} = \frac{1}{2}(R_{24} + R_{23} - R_{34})$$
$$R_{L1} = \frac{1}{2}(R_{01} + R_{12} - R_{02}) \qquad R_{R3} = \frac{1}{2}(R_{34} + R_{23} - R_{24})$$
$$R_{L0} = \frac{1}{2}(R_{01} + R_{02} - R_{12}) \qquad R_{R4} = \frac{1}{2}(R_{34} + R_{24} - R_{23}).$$

A. One-DoF Data Modeling

We employed three regression models for deformation prediction to enhance the accuracy and reduce noise in our measurements. Here, we used the bending angle ($\hat{y}$) to quantify the deformation level, as the bending angle can be standardized by our test setup. The selected resistance measurements (R_{L2}, R_{R2}, R_{L1}, R_{R3}, R_{L0}, and R_{R4}), and several derived features serve as effective predictors in our analysis.

The data models we proposed are: the raw signal linear model (1), the ratio model (2)], and the hybrid model (3). Each model uniquely combines these sub-segments and derived features to provide a comprehensive approach to angle prediction

$$\hat{y_1} = p_0 + p_1(R_{L2}) + p_2(R_{R2}) + p_3(R_{L1}) + p_4(R_{R3}) + p_5(R_{L0}) + p_6(R_{R4}) \quad (1)$$

$$\hat{y_2} = q_0 + q_1\left(\frac{R_{L2}}{R_{R2}}\right) + q_2\left(\frac{R_{L1}}{R_{R3}}\right) + q_3\left(\frac{R_{L0}}{R_{R4}}\right) \quad (2)$$

$$\hat{y_h} = s_0 + s_1(\hat{y_1}) + s_2(\hat{y_2}). \quad (3)$$

For these equations, $p_i, q_j, s_k \in \mathbb{R}$, where $i \in [0, 6]$, $j \in [0, 3]$, $k \in [0, 2]$, and $i, j, k \in \mathbb{N} \geq 0$.

These equations are employed for estimating angles in systems with one DoF. However, a system with two sensing locations experiencing 2-D bending would constitute four-DoFs. In such cases, we utilize the current bending angle as an input for estimating further DoFs, as detailed in Section IV-B.

B. Multideformation Data Modeling

In multideformation scenarios, often involving two or three bending angles, we propose a cascaded linear regression model approach. This cascaded approach reflects the inherent correlation between angles x and y in the sensor's design, where deformation at one location influences the other due to shared mechanical and electrical pathways (see Fig. 3). For predicting two angles, x and y, we represent them as vector data points $\mathbf{x}_{(n\times 1)}$ and $\mathbf{y}_{(n\times 1)}$.

Initially, a linear regression model is trained to predict angle y, using a matrix of test samples $\mathbf{D}_{\mathbf{y}(n\times p)}$ and coefficients $\mathbf{w}_{\mathbf{y}(p\times 1)}$. For angle x, we train multiple models, each tailored to a range of y, by segmenting the training set into m bins based on y. Each bin's model, defined by coefficients $\mathbf{w}_{\mathbf{x}(q_j\times 1)}^{j}$ and test data $\mathbf{D}_{\mathbf{x}(n_j\times q_j)}^{j}$, predicts x more precisely.

The testing phase is a two-step process: predicting y first, then x using the bin-specific model corresponding to the

[3]https://acrylictech.com.au/product/acri-bond-105-2/

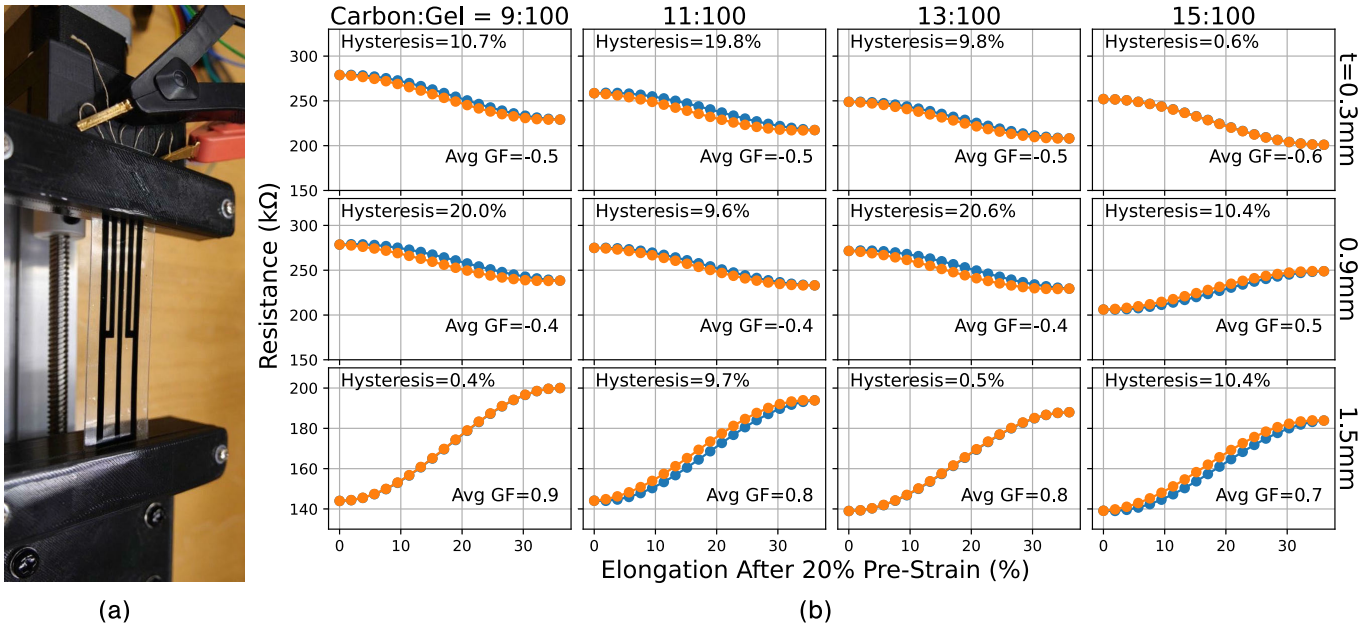

Fig. 4. (a) Stretching test setup: sample clamping and measurement are shown. (b) Resistance variation versus elongation percentage for different carbon–gel weight ratios and conductive layer thicknesses. The maximum hysteresis and GF are indicated at each subplot's top left and bottom right.

predicted y. This cascaded model approach, with its focus on bin-specific models, enhances prediction accuracy in complex multideformation situations.

V. Evaluation

A. Sensing Strategy and Material Evaluation

In our pilot study, we observed that the samples' initial stretch did not always exhibit a monotonic resistance change. This aligns with findings from Yamaguchi et al. [60] and López-de-Uralde et al. [61], who reported nonmonotonic resistivity behavior due to microstructural rearrangements. To address this, we applied a prestrain strategy (applying 20% initial strain) to bypass the unstable region, ensuring repeatable resistance-strain behavior for sensing.

Other critical parameters like conductivity, gauge factor (GF), and hysteresis are also key in defining the performance of resistive sensors [62], [63]. Our investigation focuses on determining the optimal weight ratio of carbon powder to gel and the ideal conductive layer thickness, aiming to balance these sensors' precision and accuracy effectively.

1) Procedure: We conducted stretching tests on 12 samples with varying carbon/gel ratios and thicknesses, subjecting them to 1000 cycles using a linear actuator [see Fig. 4(a)]. This assessed their performance after 20% prestrain. Empirical evidence suggests that carbon/gel ratios below 9:100 or above 15:100 lead to nonideal conductivity or the formation of cracks in cured conductive substrates. Consequently, we selected four carbon/gel ratios ranging from 9:100 to 15:100 and three conductive layer thicknesses (0.3, 0.9, and 1.5 mm). The weight of samples was precisely measured using a high-precision scale,[4] and the thickness of the conductive layers was standardized using 300-μm acrylic sheets as spacers.

2) Results: In Fig. 4(b), we observed a nonconstant direction in resistance change with varying weight ratios and thicknesses. Specifically, resistance decreases upon elongation at a thickness of 0.3 mm, whereas at 1.5 mm, it exhibits an increasing trend. In addition, each plot exhibits monotonic but nonlinear characteristics. To quantify sensitivity, we define the averaged GF (Avg GF) as follows:

$$Avg\ GF = \frac{1}{\varepsilon_{\max}} \int_0^{\varepsilon_{\max}} \frac{dR/R}{d\varepsilon}\, d\varepsilon \tag{4}$$

where $\varepsilon_{\max} = 0.36$ (36% elongation), R is resistance, and $d\varepsilon$ represents incremental strain. This formulation averages the sensitivity across the working range.

Analysis demonstrates that the 15:100 carbon/gel ratio at 0.3-mm thickness offers lower hysteresis (0.6%) and a higher magnitude of Avg GF (0.6), making it suitable for epidermal sensors. Although a 1.5-mm thickness layer shows the largest magnitude in Avg GF (0.9) with the lowest hysteresis (0.4%), it is excessively thick for epidermal applications [15]. Consequently, we selected a 15:100 carbon/gel weight ratio and a 0.3-mm thickness for the conductive layer.

VI. Multi-DoF Sensing Pattern Simulation

Building on square multi-DoF sensor design, we established the sensing principles and data collection methods for a single design. This section explores additional patterns that could enhance the sensor's DoFs and overall accuracy.

As depicted in Fig. 5(m)–(o), we utilized Ansys Mechanical APDL[5] to simulate strain changes in each trace. Subsequently,

[4] instrumentchoice.com.au/1kg-digital-bench-scale-001g-resolution-ic-7264
[5] https://www.ansys.com/

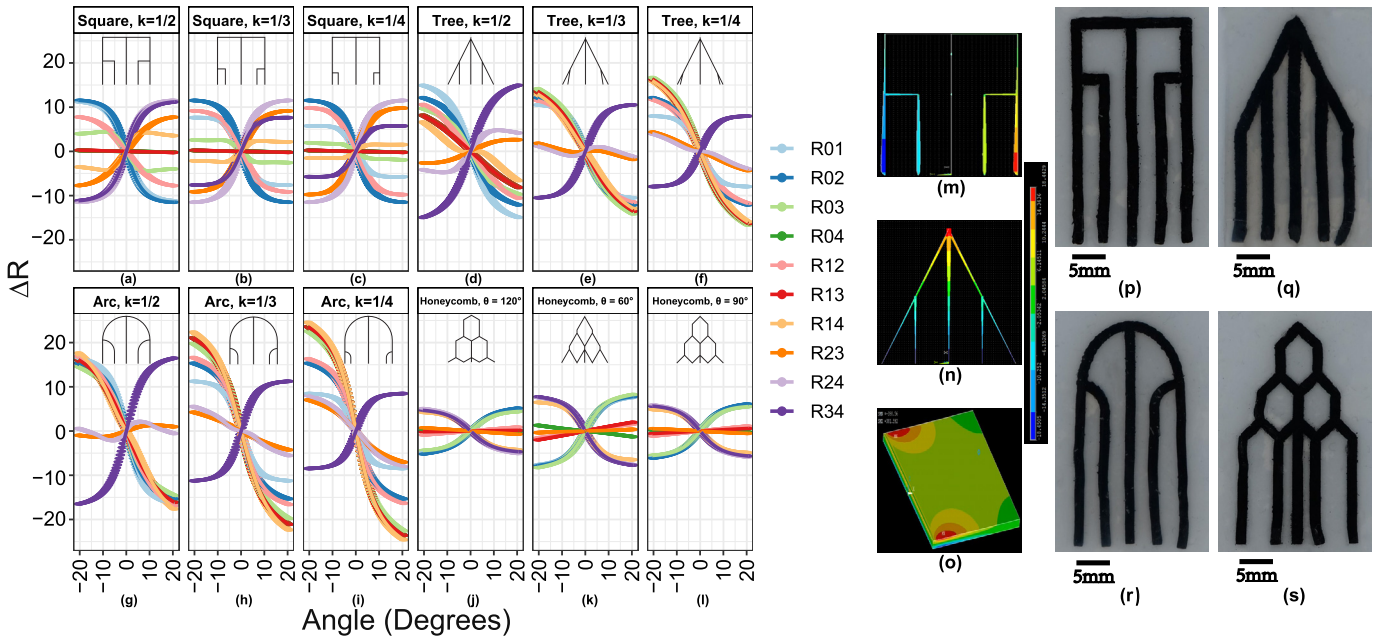

Fig. 5. Resistance variations analysis in the proposed patterns under horizontal bending. (a)–(c) Square-like pattern. (d)–(f) Tree-like pattern. (g)–(i) Arc-like pattern. (j)–(l) Honeycomb-like pattern. Simulations of (m) square-like pattern, (n) tree-like pattern, and (o) horizontal bending with a sensor (unit: Newton). (p)–(s) Four multi-DoF sensing patterns after fabrication.

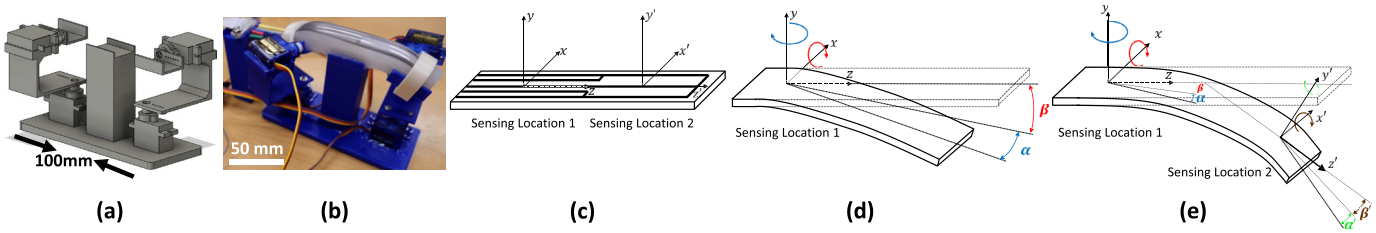

Fig. 6. (a) 3-D model of test setup. (b) Real testing photo of the finger-like test setup. Schematics the test setup. (c) Simplified view with the sensor positioned on top. (d) Deformation in locations 1. (e) Deformation in both locations 1 and 2.

we incorporated empirical data from Sections V-A and VI-A to compute the resistance values for each trace (e.g., R_{01}, R_{02}, and R_{03}). This simulation encompassed four types of multi-DoF sensing patterns, each comprising three variations. The outlines of these sample shapes are illustrated at the top of Fig. 5(a)–(l). In this context, "k" represents the ratio of the size of each subsequent pattern level to the last level of length or area. In addition, "θ" denotes the smallest angle within each hexagon in the honeycomb-like pattern. We subjected the samples to a horizontal bending simulation, ranging from $-20°$ to $+20°$. The resistance changes observed for each trace, as a result of this bending, are detailed in Fig. 5(a)–l).

The results, as illustrated in Fig. 5(a)–(i), reveal that a smaller "k" tends to produce a higher resistance change, despite their overall similar performance. Moreover, as shown in Fig. 5(j)–(l), the GFs for honeycomb-like designs with θ values of 120°, 90°, and 60° increase. The amplitude ranking from high to low is arc, tree, square, and honeycomb. The honeycomb shapes have multiple parallel circuits, which reduces their resistance. As for the remaining three designs, we conclude that the sharper corners or turnings a design has in the circuit, the larger its resistance change, because a curly trace generally increases resistance.

In addition, we found that the resistance between points 1 and 3 (R13) under horizontal bending exhibits distinct behavior across multi-DoF designs. All data were obtained after applying a 20% prestrain to stabilize the conductive network. In square and honeycomb patterns, two corner traces (top left and top right) exhibit compensatory behavior—one trace's resistance increases while the other decreases—resulting in flatter resistance. Conversely, in arc and tree patterns, the current path between R13 traces aligns tangentially to the applied force, amplifying strain-induced resistance changes and producing nonflat R13 curves. This highlights how geometric design governs strain distribution and current-path alignment in multi-DoF sensing.

A. Performance Evaluations

To assess the effectiveness of our proposed multi-DoF sensing patterns, we initially focused on the square pattern depicted in Fig. 3 for performance evaluation. Our test setup, as illustrated in Fig. 6(a), includes four servo motors to simulate four DoFs in bending. The silicone–gel cylinder with embedded 3-D-printed bones, as shown in Fig. 6(b), closely mimics the texture and internal structure of a finger. As shown in Fig. 6(b), we bonded the epidermal sensor to

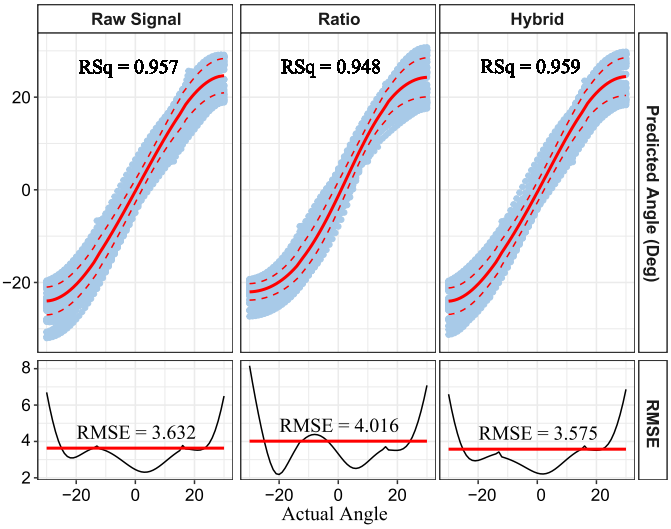

Fig. 7. Model comparison for sensing location 1 in horizontal bending: model-predicted versus actual angles (top) and RMSE variations versus actual angles (bottom).

this set-up. The sensor features two distinct sensing locations, each capable of detecting deformations of the x- and y-axis. In this context, the horizontal and vertical bending in the sensing locations 1 and 2 are represented as α, β, α', and β', respectively. All the collected data are employed in an 80–20 training–testing split with tenfold cross-validation on the training data.

B. Evaluation of Sensing Location 1

In this section, we focus on evaluating x- and y-axis deformation in sensing location 1, primarily examining horizontal bending as vertical bending closely aligns with material evaluations discussed in Section V-A. The goal is to identify the most effective model, the raw signal model, the ratio model, or the hybrid model for accurately predicting bending angles. We evaluated these models using their R^2 (RSq) and RMSE values. A higher value of R^2 indicates better predictive accuracy, while a lower RMSE suggests a reduced deviation from the predicted values.

Comparative analyses of the models, as shown in Fig. 7, reveal that the hybrid model generally achieves the highest R^2 value, closely followed by the raw signal model. This indicates effective predictions of horizontal bending in sensing location 1 by both models. However, for higher precision, we opt for the hybrid model in subsequent evaluations. Moreover, we observed a significant increase in RMSE values when the bending exceeded an absolute threshold of 25°. We achieve a high-precision horizontal bending range of $\alpha \in [-30°, 30°]$, as RMSE within this range remains below the threshold. Applying the same criteria, the high-precision range for vertical bending in sensing location 1 is determined as $\beta \in [-75°, 0°]$. These defined ranges will guide our subsequent evaluation studies.

C. Evaluation of Both Sensing Locations 1 and 2

To evaluate our design's performance with higher DoFs, we employed hybrid models to predict the x- and y-axis

	Vertical Bending 1 (β)	Horizontal Bending 1 (α)	Vertical Bending 2 (β′)	Horizontal Bending 2 (α′)
R^2	0.989	0.959	0.903	0.861
Standard Deviation	0.666°	0.945°	1.200°	1.399°
High-precision Range	[-75°, 0°]	[-30°, 30°]	[-60°, 0°]	[-25°, 25°]

Fig. 8. Table of Metric Performance Across Four DoFs (α, β, α', and β').

movements in sensing locations 1 and 2. It is widely recognized that multi-deformation sensing locations correspond to complex finger bending motions. As illustrated in Fig. 8, the performance metrics in sensing location 2 (α' and β') are slightly inferior to those in sensing location 1 (α and β). This is evidenced by lower R^2 values and a reduced high-precision range, suggesting that an increase in the number of sensing DoFs may lead to a decrease in performance. Nonetheless, the R^2 values of 90.3% for vertical bending and 86.1% for horizontal bending at sensing location 2 are still notable [64], which demonstrate reliable performance. Furthermore, the four-DoF sensor demonstrates a standard deviation of $\sigma = 1.399°$. Based on the properties of the normal distribution [65], 95.4% of the sensor's angular measurements lie within $\pm 2\sigma$ ($\pm 2.798°$) of the actual value. This confidence interval indicates that the sensor's output deviates from ground truth by no more than $\pm 2.798°$ for 95.4% of observations. To improve performance, future efforts could focus on refining calibration methods, such as optimizing pattern recognition algorithms for targeted applications to minimize the measurement variability.

VII. Discussion

In this article, we presented four patterns for multi-DoF deformation sensing. Our study focused on assessing its effectiveness through both a finger-like test setup and simulation analysis. The findings confirm the reliability of these patterns, particularly the square-like designs, in both practical and simulated environments. These designs use a single conductive layer to approximate multidirectional deformation. This approach is particularly beneficial in situations with limited access to advanced equipment and where sensor thickness is a critical factor. Our approach enables rapid prototyping and predictable fabrication of epidermal sensors, making a valuable contribution to the field.

A key advancement lies in our fabrication technique. By layering acrylic sheets with adhesive, we effectively control sensor thickness without relying on sophisticated machinery. Furthermore, we propose a novel approach to thickness control in bending sensor fabrication: using paper layers (approximately 25 μm each) as a frame in the mold. This technique allows for ultrathin substrates, with precision up to 25μm. This method stands in contrast to the expensive thin-film applicators or spin-coaters used in previous studies, such as by Weigel et al. [18]. Our approach, leveraging common materials like paper, is both cost-effective and widely

accessible, making it a viable option for most fabrication laboratories.

In our experiments, we observed that the resistance (R) of some carbon-doped elastomers initially increases and then decreases under strain, though not all samples follow this trend. From the formula $R = \rho L/A$, stretching increases length (L) while reducing cross-sectional area (A), implying that L/A should rise monotonically. However, prior work by Yamaguchi et al. [60] demonstrated nonmonotonic resistivity changes in carbon-polymer composites. Through material evaluation, we found that sensors with thinner thickness and lower carbon ratios are more likely to exhibit downward resistance trends, while thicker sensors with higher carbon ratios follow the expected L/A-driven behavior. This suggests that resistivity (ρ) changes dominate in thinner/low-carbon sensors, whereas geometric effects (L, A) prevail in thicker/high-carbon cases. While our setup lacks the capability for microstructural validation (e.g., SEM/TEM), future work will explore filler network dynamics to resolve this.

This article demonstrates a multi-DoF epidermal sensor on a finger, including its actual data collection capabilities. When users customize their sensors, tangential traces, force direction, and sharp circuit corners should be taken into consideration to increase sensing amplitude and GFs. Moreover, users can optimize the sensor for different finger joints, and customize the number of fingers or joints to use, as demonstrated in projects with three [66] or six fingers [67]. Our findings show that a smaller number of joints indicates fewer variables needed for sensing. This yields more accurate numerical results under the same computational resources. Therefore, if we can identify appropriate frequencies for joint use from previous research, we can reduce the fabrication of some joints in the sensor, achieving more precise motion prediction. We anticipate that these designs will advance the development of multi-DoF deformation sensors.

VIII. Limitations and Future Work

While our study presents significant advancements, it also uncovers certain limitations that pave the way for future research. First, we observed a marginal decrease in sensing accuracy (about 5%) with the addition of extra sensing locations. Although this reduction is not substantial, it does affect the sensor's ability to detect multiple DoFs accurately. Future research should explore the use of more advanced materials (e.g., hybrid conductive fillers) [68], the optimal ratio of conductive elements, and more suitable learning algorithms to minimize this error rate.

Second, when users wear the sensors for the first time, they have to perform an on-the-fly calibration [35] to compensate for the hysteresis problem, which may undermine the user experience. Future efforts will be directed toward developing advanced circuitry and algorithms to further compensate for the hysteresis, enhancing the overall accuracy and reliability of the sensors.

Third, the time taken for sensor fabrication is another area for improvement. Achieving consistency in material mixes and maintaining accurate ratios during the fabrication process present challenges that future research will need to address.

In summary, future work will refine our sensor design by optimizing materials, compensating for hysteresis, and streamlining the fabrication process. These improvements aim to enhance the sensor's performance and usability and could also potentially help to address VR occlusion by providing an on-body signal that complements camera-based tracking, thereby improving tracking robustness, interaction continuity, and overall user comfort and immersion [69], [70], [71].

IX. Conclusion

This article explored the design and fabrication of multi-DoF epidermal bend sensors using flexible resistive patterns. Our method was inspired by traditional uniaxial sensors, but instead achieves multi-DoF sensing. The approach combines resistive sensing techniques with accessible fabrication methods to create deformation sensors. In addition, we showcased a four-DoF sensor with 95.4% of measurements falling within $\pm 2.798°$ of ground truth. We also demonstrated comprehensive experimental validation for the proposed multi-DoF sensing patterns. Future work will aim to further refine the fabrication process and material optimization. Overall, this research contributes to advancing wearable sensor technology, combining innovation with practical, accessible design and setting the stage for developments in soft and conformal sensing.

Acknowledgment

The authors acknowledge Jing Zeng for figure polishing and insightful suggestions. In addition, they also appreciate the members of the AID-LAB for assisting them in various ways.

References

[1] L. J. Currano, F. C. Sage, M. Hagedon, L. Hamilton, J. Patrone, and K. Gerasopoulos, "Wearable sensor system for detection of lactate in sweat," *Sci. Rep.*, vol. 8, no. 1, pp. 1–11, Oct. 2018.

[2] H.-R. Lim, H. S. Kim, R. Qazi, Y.-T. Kwon, J.-W. Jeong, and W.-H. Yeo, "Advanced soft materials, sensor integrations, and applications of wearable flexible hybrid electronics in healthcare, energy, and environment," *Adv. Mater.*, vol. 32, no. 15, Apr. 2020, Art. no. 1901924.

[3] S. Russo, T. Ranzani, H. Liu, S. Nefti-Meziani, K. Althoefer, and A. Menciassi, "Soft and stretchable sensor using biocompatible electrodes and liquid for medical applications," *Soft Robot.*, vol. 2, no. 4, pp. 146–154, Dec. 2015.

[4] M. A. Ahmed, B. B. Zaidan, A. A. Zaidan, M. M. Salih, and M. M. B. Lakulu, "A review on systems-based sensory gloves for sign language recognition state of the art between 2007 and 2017," *Sensors*, vol. 18, no. 7, p. 2208, Jul. 2018.

[5] J. Yu et al., "IrOnTex: Using ironable 3D printed objects to fabricate and prototype customizable interactive textiles," *Proc. ACM Interact., Mobile, Wearable Ubiquitous Technol.*, vol. 8, no. 3, pp. 1–26, Sep. 2024.

[6] J. K. Sim, S. Yoon, and Y.-H. Cho, "Wearable sweat rate sensors for human thermal comfort monitoring," *Sci. Rep.*, vol. 8, no. 1, pp. 1–11, Jan. 2018.

[7] D. R. Seshadri et al., "Wearable sensors for monitoring the internal and external workload of the athlete," *NPJ Digit. Med.*, vol. 2, no. 1, p. 71, 2019.

[8] J. Marín-Morales et al., "Affective computing in virtual reality: Emotion recognition from brain and heartbeat dynamics using wearable sensors," *Sci. Rep.*, vol. 8, no. 1, pp. 1–15, Sep. 2018.

[9] K. Song et al., "Pneumatic actuator and flexible piezoelectric sensor for soft virtual reality glove system," *Sci. Rep.*, vol. 9, no. 1, pp. 1–8, Jul. 2019.

[10] S.-W. Kim et al., "Thermal display glove for interacting with virtual reality," *Sci. Rep.*, vol. 10, no. 1, pp. 1–12, Jul. 2020.

[11] E. A. Susanto, R. K. Tong, C. Ockenfeld, and N. S. Ho, "Efficacy of robot-assisted fingers training in chronic stroke survivors: A pilot randomized-controlled trial," *J. NeuroEng. Rehabil.*, vol. 12, no. 1, pp. 1–9, Dec. 2015.

[12] J. Suo et al., "AI-enabled soft sensing array for simultaneous detection of muscle deformation and mechanomyography for metaverse somatosensory interaction," *Adv. Sci.*, vol. 11, no. 16, 2024, Art. no. 2305025.

[13] Y. Cheng, K. Wang, H. Xu, T. Li, Q. Jin, and D. Cui, "Recent developments in sensors for wearable device applications," *Anal. Bioanal. Chem.*, vol. 413, no. 24, pp. 6037–6057, Oct. 2021.

[14] H. Chandel and S. Vatta, "Occlusion detection and handling: A review," *Int. J. Comput. Appl.*, vol. 120, no. 10, pp. 33–38, Jun. 2015.

[15] A. S. Nittala and J. Steimle, "Next steps in epidermal computing: Opportunities and challenges for soft on-skin devices," in *Proc. CHI Conf. Human Factors Comput. Syst.*, Apr. 2022, pp. 1–22.

[16] E. Chau, J. Yu, C. Goncu, and A. Withana, "Composite line designs and accuracy measurements for tactile line tracing on touch surfaces," in *Proc. ACM Hum.-Comput. Interact.*, Nov. 2021, vol. 5, no. ISS, pp. 1–17.

[17] J. Yu, P. B. Perera, R. V. Perera, M. M. Valashani, and A. Withana, "Fabricating customizable 3-D printed pressure sensors by tuning infill characteristics," *IEEE Sensors J.*, vol. 24, no. 6, pp. 7604–7613, Mar. 2024.

[18] M. Weigel, T. Lu, G. Bailly, A. Oulasvirta, C. Majidi, and J. Steimle, "ISkin: Flexible, stretchable and visually customizable on-body touch sensors for mobile computing," in *Proc. 33rd Annu. ACM Conf. Human Factors Comput. Syst.*, Apr. 2015, pp. 2991–3000.

[19] A. S. Nittala, A. Withana, N. Pourjafarian, and J. Steimle, "Multi-touch skin: A thin and flexible multi-touch sensor for on-skin input," in *Proc. CHI Conf. Human Factors Comput. Syst.*, New York, NY, USA, Apr. 2018, pp. 1–12.

[20] H. Yuk, T. Zhang, G. A. Parada, X. Liu, and X. Zhao, "Skin-inspired hydrogel–elastomer hybrids with robust interfaces and functional microstructures," *Nature Commun.*, vol. 7, no. 1, p. 12028, Jun. 2016.

[21] T. Han et al., "HapBead: On-skin microfluidic haptic interface using tunable bead," in *Proc. CHI Conf. Human Factors Comput. Syst.*, Apr. 2020, pp. 1–10.

[22] A. Withana, D. Groeger, and J. Steimle, "Tacttoo: A thin and feel-through tattoo for on-skin tactile output," in *Proc. 31st Annu. ACM Symp. User Interface Softw. Technol.*, New York, NY, USA, Oct. 2018, pp. 365–378.

[23] M. Weigel, A. S. Nittala, A. Olwal, and J. Steimle, "SkinMarks: Enabling interactions on body landmarks using conformal skin electronics," in *Proc. CHI Conf. Human Factors Comput. Syst.*, New York, NY, USA, May 2017, pp. 3095–3105.

[24] A. K. Bose et al., "Screen-printed strain gauge for micro-strain detection applications," *IEEE Sensors J.*, vol. 20, no. 21, pp. 12652–12660, Nov. 2020.

[25] M. Caeiro-Rodríguez, I. Otero-González, F. A. Mikic-Fonte, and M. Llamas-Nistal, "A systematic review of commercial smart gloves: Current status and applications," *Sensors*, vol. 21, no. 8, p. 2667, Apr. 2021.

[26] M. Amjadi, A. Pichitpajongkit, S. Lee, S. Ryu, and I. Park, "Highly stretchable and sensitive strain sensor based on silver Nanowire–Elastomer nanocomposite," *ACS nano*, vol. 8, no. 5, pp. 5154–5163, 2014.

[27] Q. Xia et al., "Highly linear and low hysteresis porous strain sensor for wearable electronic skins," *Composites Commun.*, vol. 26, Aug. 2021, Art. no. 100809.

[28] K. Kim, J. Lee, E. Jo, S. Sim, and J. Kim, "Patterned carbon nanotube bundles as stretchable strain sensors for human motion detection," *ACS Appl. Nano Mater.*, vol. 3, no. 11, pp. 11408–11415, Nov. 2020.

[29] K. Hassan et al., "Fractal design for advancing the performance of chemoresistive sensors," *ACS Sensors*, vol. 6, no. 10, pp. 3685–3695, Oct. 2021.

[30] T. Röddiger, M. Beigl, D. Wolffram, M. Budde, and H. Sun, "PDMSkin: On-skin gestures with printable ultra-stretchable soft electronic second skin," in *Proc. Augmented Humans Int. Conf.*, 2020, pp. 1–9.

[31] N. Li, W. Zhao, F. Li, L. Liu, Y. Liu, and J. Leng, "A 4D-printed programmable soft network with fractal design and adjustable hydrophobic performance," *Matter*, vol. 6, no. 3, pp. 940–962, Mar. 2023.

[32] S. Wu, S. Peng, Y. Yu, and C.-H. Wang, "Strategies for designing stretchable strain sensors and conductors," *Adv. Mater. Technol.*, vol. 5, no. 2, Feb. 2020, Art. no. 1900908.

[33] R. Yang et al., "Ultra-sensitive, multi-directional flexible strain sensors based on an MXene film with periodic wrinkles," *ACS Appl. Mater. Interface*, vol. 15, no. 6, pp. 8345–8354, Feb. 2023.

[34] G. Yang et al., "Highly sensitive, direction-aware, and transparent strain sensor based on oriented electrospun nanofibers for wearable electronic applications," *Chem. Eng. J.*, vol. 435, May 2022, Art. no. 135004.

[35] O. Glauser, S. Wu, D. Panozzo, O. Hilliges, and O. Sorkine-Hornung, "Interactive hand pose estimation using a stretch-sensing soft glove," *ACM Trans. Graph.*, vol. 38, no. 4, pp. 1–15, Jul. 2019.

[36] O. Glauser, D. Panozzo, O. Hilliges, and O. Sorkine-Hornung, "Deformation capture via soft and stretchable sensor arrays," *ACM Trans. Graph.*, vol. 38, no. 2, pp. 1–16, Apr. 2019.

[37] C. Rendl et al., "FlexSense: A transparent self-sensing deformable surface," in *Proc. 27th Annu. ACM Symp. User Interface Softw. Technol.*, Oct. 2014, pp. 129–138.

[38] F. Shahmiri and P. H. Dietz, "ShArc: A geometric technique for multi-bend/shape sensing," in *Proc. CHI Conf. Human Factors Comput. Syst.*, New York, NY, USA, Apr. 2020, pp. 1–12.

[39] R. Adam and C. Robertson, *Screenprinting: The Complete Water-Based System*. London, U.K.: Thames & Hudson, 2003.

[40] Y. Kim, H. Kim, and H.-J. Yoo, "Electrical characterization of screen-printed circuits on the fabric," *IEEE Trans. Adv. Packag.*, vol. 33, no. 1, pp. 196–205, Feb. 2010.

[41] F. Marra, S. Minutillo, A. Tamburrano, and M. S. Sarto, "Production and characterization of graphene nanoplatelet-based ink for smart textile strain sensors via screen printing technique," *Mater. Design*, vol. 198, Jan. 2021, Art. no. 109306.

[42] A. Khan, J. S. Roo, T. Kraus, and J. Steimle, "Soft inkjet circuits: Rapid multi-material fabrication of soft circuits using a commodity inkjet printer," in *Proc. 32nd Annu. ACM Symp. User Interface Softw. Technol.*, New York, NY, USA, Oct. 2019, pp. 341–354.

[43] T. Cheng et al., "Silver tape: Inkjet-printed circuits peeled-and-transferred on versatile substrates," *Proc. ACM Interact. Mob. Wearable Ubiquitous Technol.*, vol. 4, no. 1, pp. 1–17, Mar. 2020.

[44] Y. Choi, N. Ryu, M. J. Kim, A. Dementyev, and A. Bianchi, "BodyPrinter: Fabricating circuits directly on the skin at arbitrary locations using a wearable compact plotter," in *Proc. 33rd Annu. ACM Symp. User Interface Softw. Technol.*, New York, NY, USA, Oct. 2020, pp. 554–564.

[45] N. Pourjafarian et al., "BodyStylus: Freehand on-body design and fabrication of epidermal interfaces," in *Proc. CHI Conf. Human Factors Comput. Syst.*, New York, NY, USA, May 2021, pp. 1–15.

[46] D. Groeger and J. Steimle, "LASEC: Instant fabrication of stretchable circuits using a laser cutter," in *Proc. CHI Conf. Human Factors Comput. Syst.*, New York, NY, USA, May 2019, pp. 1–14.

[47] M. Signer, A. Ion, and O. Sorkine-Hornung, "Developable metamaterials: Mass-fabricable metamaterials by laser-cutting elastic structures," in *Proc. CHI Conf. Human Factors Comput. Syst.*, New York, NY, USA, May 2021, pp. 1–13.

[48] H.-L. C. Kao, C. Holz, A. Roseway, A. Calvo, and C. Schmandt, "DuoSkin: Rapidly prototyping on-skin user interfaces using skin-friendly materials," in *Proc. ACM Int. Symp. Wearable Comput.*, Sep. 2016, pp. 16–23.

[49] N. Lu, "'Cut-and-paste' manufacture of multiparametric epidermal electronic systems," *SPIE Newsroom*, pp. 6423–6430, Jul. 2016.

[50] Y. Wang et al., "AnimSkin: Fabricating epidermis with interactive, functional and aesthetic color animation," in *Proc. Conf. Designing Interact. Syst.*, New York, NY, USA, Jun. 2017, pp. 397–401.

[51] Y. Luo et al., "Flexible liquid metal-based microfluidic strain sensors with fractal-designed microchannels for monitoring human motion and physiological signals," *Biosensors Bioelectron.*, vol. 246, Feb. 2023, Art. no. 115905.

[52] C. Vu, T. Truong, and J. Kim, "Fractal structures in flexible electronic devices," *Mater. Today Phys.*, vol. 27, Oct. 2022, Art. no. 100795.

[53] W. Wang, Y. Sun, Y. Lu, J. Wang, Y. Cao, and C. Zhang, "Tensile behavior of bio-inspired hierarchical suture joint with uniform fractal interlocking design," *J. Mech. Behav. Biomed. Mater.*, vol. 113, Jan. 2021, Art. no. 104137.

[54] J. A. Fan et al., "Fractal design concepts for stretchable electronics," *Nature Commun.*, vol. 5, no. 1, p. 3266, Feb. 2014.

[55] F. E. Lennon et al., "Lung cancer—A fractal viewpoint," *Nature Rev. Clin. Oncol.*, vol. 12, no. 11, pp. 664–675, 2015.

[56] E. R. Weibel, "Fractal geometry: A design principle for living organisms," *Amer. J. Physiol.-Lung Cellular Mol. Physiol.*, vol. 261, no. 6, pp. L361–L369, Dec. 1991.

[57] *SYLGARD 184 Silicone Elastomer APPLICATIONS*, The Dow Chemical Company, Midland, MI, USA, 2017.

[58] P. Humbert, H. I. Maibach, F. Fanian, and P. Agache, *Agache's Measuring the Skin*. Cham, Switzerland: Springer, 2017.

[59] M. Tavakoli et al., "Carbon doped PDMS: Conductance stability over time and implications for additive manufacturing of stretchable electronics," *J. Micromech. Microeng.*, vol. 27, no. 3, Feb. 2017, Art. no. 035010.

[60] K. Yamaguchi, J. J. C. Busfield, and A. G. Thomas, "Electrical and mechanical behavior of filled elastomers. I. The effect of strain," *J. Polym. Sci. B, Polym. Phys.*, vol. 41, no. 17, pp. 2079–2089, Sep. 2003.

[61] J. López-de-Uralde et al., "Automatic morphological categorisation of carbon black nano-aggregates," in *Proc. Int. Conf. Database Expert Syst. Appl.*, Aug. 2010, pp. 185–193.

[62] Y.-T. Wu, T. Yan, and Z.-J. Pan, "Wearable carbon-based resistive sensors for strain detection: A review," *IEEE Sensors J.*, vol. 21, no. 4, pp. 4030–4043, Feb. 2021.

[63] J. Shintake, Y. Piskarev, S. H. Jeong, and D. Floreano, "Ultrastretchable strain sensors using carbon black-filled elastomer composites and comparison of capacitive versus resistive sensors," *Adv. Mater. Technol.*, vol. 3, no. 3, Mar. 2018, Art. no. 1700284.

[64] T. Morikawa, N. Mura, T. Sato, and H. Katoh, "Validity of the estimated angular information obtained using an inertial motion capture system during standing trunk forward and backward bending," *BMC Sports Sci., Med. Rehabil.*, vol. 16, no. 1, p. 154, Jul. 2024.

[65] H. T. Nguyen, V. Kreinovich, and C.-W. Tao, "Why 95% and two sigma? A theoretical justification for an empirical measurement practice," Tech. Rep., 2000.

[66] K. Amano, Y. Iwasaki, K. Nakabayashi, and H. Iwata, "Development of a three-fingered jamming gripper for corresponding to the position error and shape difference," in *Proc. 2nd IEEE Int. Conf. Soft Robot. (RoboSoft)*, Apr. 2019, pp. 137–142.

[67] D. Prattichizzo, M. Malvezzi, I. Hussain, and G. Salvietti, "The sixth-finger: A modular extra-finger to enhance human hand capabilities," in *Proc. 23rd IEEE Int. Symp. Robot Human Interact. Commun.*, Aug. 2014, pp. 993–998.

[68] G. Yun, S.-Y. Tang, H. Lu, S. Zhang, M. D. Dickey, and W. Li, "Hybrid-filler stretchable conductive composites: From fabrication to application," *Small Sci.*, vol. 1, no. 6, Jun. 2021, Art. no. 2000080.

[69] T. Li, E. Velloso, A. Withana, and Z. Sarsenbayeva, "Estimating the effects of encumbrance and walking on mixed reality interaction," in *Proc. CHI Conf. Human Factors Comput. Syst.*, New York, NY, USA, Apr. 2025, pp. 1–24.

[70] T. Li, E. Velloso, A. Withana, and Z. Sarsenbayeva, "Weight-induced consumed endurance (WICE): A model to quantify shoulder fatigue with weighted objects," in *Proc. 38th Annu. ACM Symp. User Interface Softw. Technol.*, Sep. 2025, pp. 1–15.

[71] D. Ma et al., "AvaTTAR: Table tennis stroke training with embodied and detached visualization in augmented reality," in *Proc. 37th Annu. ACM Symp. User Interface Softw. Technol.*, Oct. 2024, pp. 1–16.